Nano Research
DOI 10.1007/s12274-017-1537-z
Research Article
ISSN 1998-0124
CN 11-5974/O4

$FeSe_2$ clusters with excellent cyclability and rate capability for sodium-ion batteries

Xiujuan Wei[1], Chunjuan Tang[1,2], Qinyou An[1] (✉), Mengyu Yan[1], Xuanpeng Wang[1], Ping Hu[1], Xinyin Cai[1], and Liqiang Mai[1,3] (✉)

[1] *State Key Laboratory of Advanced Technology for Materials Synthesis and Processing, Wuhan University of Technology, Wuhan 430070, China*
[2] *Department of Mathematics and Physics, Luoyang Institute of Science and Technology, Luoyang 471023, China*
[3] *Department of Chemistry, University of California, Berkeley, California 94720, USA*

Received: 20 December 2016
Revised: 25 January 2017
Accepted: 13 February 2017

KEYWORDS
$FeSe_2$ clusters,
superior rate capability,
excellent cycling stability,
sodium-ion batteries,
pseudocapacitive behavior

ABSTRACT

Sodium-ion batteries (SIBs) have great promise for sustainable and economical energy-storage applications. Nevertheless, it is a major challenge to develop anode materials with high capacity, high rate capability, and excellent cycling stability for them. In this study, $FeSe_2$ clusters consisting of nanorods were synthesized by a facile hydrothermal method, and their sodium-storage properties were investigated with different electrolytes. The $FeSe_2$ clusters delivered high electrochemical performance with an ether-based electrolyte in a voltage range of 0.5–2.9 V. A high discharge capacity of 515 mAh·g^{-1} was obtained after 400 cycles at 1 A·g^{-1}, with a high initial columbic efficiency of 97.4%. Even at an ultrahigh rate of 35 A·g^{-1}, a specific capacity of 128 mAh·g^{-1} was achieved. Using calculations, we revealed that the pseudocapacitance significantly contributed to the sodium-ion storage, especially at high current rates, leading to a high rate capability. The high comprehensive performance of the $FeSe_2$ clusters makes them a promising anode material for SIBs.

1 Introduction

Currently, electrical energy storage plays an important role in our daily lives. As efficient energy-storage devices, lithium-ion batteries (LIBs) are widely used in portable devices and are expected to power electric vehicles owing to their high energy density and long cycle life [1–3]. However, concerns regarding the limited resources and growing cost of lithium have prompted researchers to seek alternative solutions for sustainable energy storage [4, 5]. Recently, sodium-ion batteries (SIBs) have attracted considerable attention as a substitute for LIBs because of their low cost and natural abundance [6–12]. Many cathode materials, such as $Na_3V_2(PO_4)_3$ [13], $Na_{1.25}V_3O_8$ [14], $Na_2Fe_2(SO_4)_3$ [15], and Prussian blue materials [16], have been investigated for SIBs. SIB cathode materials have exhibited remarkable performances [13–15]. Nevertheless, it is a major challenge to develop high-performance anode materials for SIBs.

Address correspondence to Liqiang Mai, mlq518@whut.edu.cn; Qinyou An, anqinyou86@whut.edu.cn

To date, SIB anode materials based on intercalation [17–21], alloying [22–25], and conversion reactions [26–28] have been proposed. Materials with insertion–extraction mechanisms exhibit good cycling performance, but their specific capacity is not high [17, 18]. Thus, considerable attention has been paid to high-capacity anode materials with alloying and conversion mechanisms. Among these, transition metal sulfides and selenides have attracted significant attention owing to their low cost, high capacity, and environmental benignity [11, 29–34]. Previous studies have focused on the fabrication of carbon-assisted composites to improve the electrochemical performance [31, 32]. However, carbon materials exhibit a low tapping density, which leads to a low practical volumetric energy density. Therefore, it is necessary to explore novel strategies for developing high-performance transition metal sulfides and selenides without introducing conductive carbon materials. $FeSe_2$ has been extensively studied in a variety of fields, e.g., those concerning solar cells [35], absorption [36] and electromagnetics [37], owing to its environmental benignity, low cost, and good conductivity. Chen et al. synthesized $FeSe_2$ microspheres and used them for the first time as an SIB anode [38]. The $FeSe_2$ anode delivered a stable discharge capacity of 372 $mAh{\cdot}g^{-1}$ at 1 $A{\cdot}g^{-1}$. However, the specific capacity and rate performance of the $FeSe_2$ SIB anode needs to be further enhanced.

Three-dimensional (3D) structures composed of sub-nanostructures have attracted attention as efficient electrode configurations [39–41]. They can not only reduce the ion diffusion length but also mitigate the self-aggregation of low-dimensional nanostructures; thus, they are used to enhance the electrochemical performance of batteries [39]. In addition, pseudocapacitive charge storage is beneficial for achieving a high rate capability [42–44]. Huang et al. [43] demonstrated that the Na^+ intercalation pseudocapacitance in graphene-coupled titanium oxide yielded a high rate capability and long cycle life in SIBs. Thus, it is desirable to obtain SIBs with a high rate capability and excellent cycling stability by constructing a 3D structure and enhancing the pseudocapacitive charge storage process in the electrodes.

In this study, we constructed $FeSe_2$ clusters assembled by nanorods using a facile hydrothermal reaction. The unique 3D structures reduced the ion diffusion length, mitigating the sluggish electrochemical kinetics. Quantitative kinetics analysis revealed that the pseudocapacitive charge storage significantly contributed to the sodium-ion storage. As an SIB anode, the as-prepared $FeSe_2$ clusters exhibited high rate performance, high initial Coulombic efficiency, and stable cycling performance.

2 Experimental

2.1 Material synthesis

The $FeSe_2$ clusters (C-$FeSe_2$) were synthesized as follow. $(NH_4)_2Fe(SO_4)_2$ (1 mmol) were added to distilled water (30 mL) under stirring. Then, SeO_2 (2 mmol) and hydrazine hydrate (6 mL) were sequentially added to the resulting mixture. Finally, the obtained solution was transferred into a Teflon-lined stainless-steel autoclave and maintained at 180 ℃ for 12 h. The product was collected via centrifugation, washed with distilled water and ethanol, and dried at 70 ℃ for 12 h in vacuum. For comparison, $FeSe_2$ particles (P-$FeSe_2$) were synthesized using the same procedure with hydrazine hydrate (3 mL). Furthermore, time-dependent experiments were performed to investigate the growth process of the $FeSe_2$ clusters.

2.2 Characterization

X-ray diffraction (XRD) patterns were recorded using a D8 Advance X-ray diffractometer with a non-monochromated Cu Kα X-ray source. Raman spectra were obtained using a micro-Raman spectroscopy system (inVia, Renishaw). Field-emission scanning electron microscopy (FESEM) images and energy-dispersive X-ray spectra (EDS) were obtained using a microscope (JEOL-7100F). Transmission electron microscopy (TEM) images and high-resolution TEM (HRTEM) images were obtained using another microscope (JEM-2100F).

2.3 Electrochemical measurements

The electrochemical properties were measured by assembling 2016 coin cells in a glove box filled with pure argon gas. Sodium chips were used as the counter

electrode. The working electrode was obtained by mixing the as-prepared materials, acetylene black, and carboxyl methyl cellulose at a weight ratio of 70:20:10. The slurry was cast on copper foil, dried at 70 °C for 12 h, and heated at 120 °C for 2 h in a vacuum oven. The active material loaded on the copper foil was 1.0–1.5 mg·cm^{-2}. Three different electrolytes were used: 1 M $NaCF_3SO_3$ dissolved in diethyleneglycol dimethylether (DIGLYME), 1 M $NaClO_4$ in ethylene carbonate and dimethyl carbonate (EC/DMC), and 1 M $NaClO_4$ in EC/DMC with 5% fluoroethylene carbonate (FEC) electrolytes. Galvanostatic charge/discharge measurements were performed in a potential range of 0.5–2.9 V vs. Na^+/Na using a multichannel battery testing system (LAND CT2001A). Cyclic voltammetry (CV) and electrochemical impedance spectroscopy (EIS) were performed using electrochemical workstations (CHI600D and Autolab Potentiostat Galvanostat 302N). All of the measurements were performed at room temperature.

3 Results and discussion

3.1 Structural characterization

As shown in Fig. 1(a) and Fig. S1 in the Electronic Supplementary Material (ESM), the XRD peak for the obtained $FeSe_2$ clusters and particles is indexed to the orthorhombic phase of $FeSe_2$ (JCPDS card No. 01-079-1892). The Raman spectrum of as-prepared $FeSe_2$ clusters is shown in Fig. 1(b). Three characteristic peaks at 179.2, 216.3, and 254.4 cm^{-1} are observed. The peaks at 179.2 and 254.4 cm^{-1} correspond to the Se–Se librational and stretching vibrations or their combination, and the peak at 216.3 cm^{-1} is attributed to the Se–Se stretching vibrations [36]. The morphology of the as-prepared $FeSe_2$ clusters was characterized using scanning electron microscopy (SEM) and TEM. The low-magnification SEM image shown in Fig. S2 in the ESM indicates that the as-prepared 3D $FeSe_2$ clusters had a diameter of 500–800 nm. Elemental-mapping images were obtained to determine the chemical composition of the as-prepared $FeSe_2$ clusters (Fig. S3 in the ESM). The elements Se and Fe were uniformly distributed in the obtained product. The EDS results show that the atomic ratio of Fe/Se was approximately 1:2. The high-magnification SEM image shown in Fig. 2(a) indicates that the $FeSe_2$ clusters were composed of nanorods. The HRTEM image shown in Fig. 2(b) indicates that the nanorods had a diameter of 100–150 nm. A lattice fringe with a *d*-spacing of approximately 0.37 nm, which corresponds to the (110) plane of the $FeSe_2$ crystal, is observed in the HRTEM image of Fig. 2(c). The selected-area electron diffraction (SAED) pattern shown in Fig. 2(d) is indexed to the (110) and (121) crystal planes of the orthorhombic $FeSe_2$ phase. The morphology of the $FeSe_2$ particles was investigated using SEM (Fig. S4 in the ESM), revealing that some nanoparticles aggregated to form larger particles.

To investigate the formation process of the obtained $FeSe_2$ clusters, time-dependent experiments were performed. The morphologies of the prepared samples at different stages were characterized using SEM (Fig. S5 in the ESM). When the reaction time was 1 h, irregular nanoparticles and rods formed. When the reaction time was extended to 3 h, obvious rod clusters appeared. After 6 h of reaction, the rods were longer.

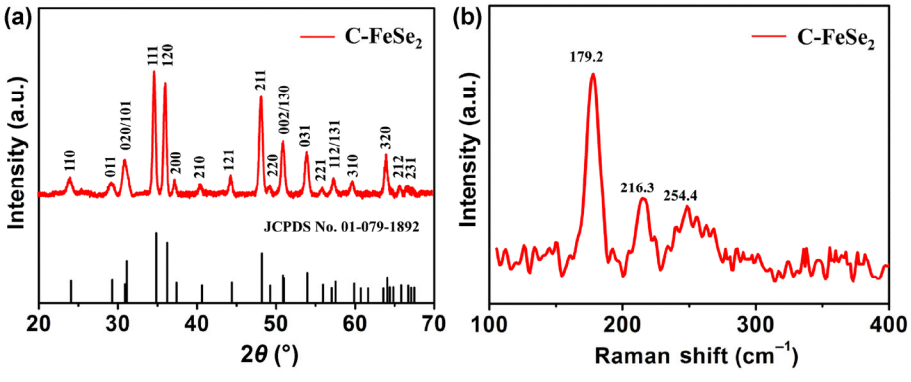

Figure 1 (a) XRD pattern and (b) Raman spectrum of the as-prepared $FeSe_2$ clusters.

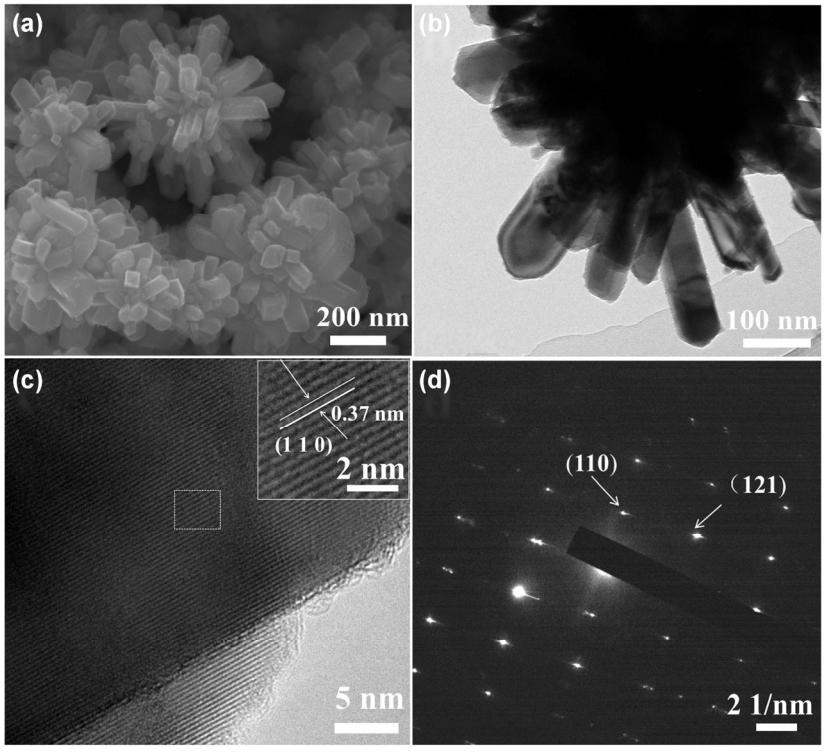

Figure 2 (a) SEM image, (b) high-magnification TEM image, (c) HRTEM image, and (d) SAED pattern of the as-prepared $FeSe_2$ clusters.

As the reaction time increased to 8 h, the particles existing on the rods were consumed, and the rod clusters became larger.

According to the aforementioned experimental results, the growth process of the obtained $FeSe_2$ clusters was schematically illustrated, as shown in Fig. S6 in the ESM. In the initial stage, nanoparticles and rods formed. As the reaction continued, particles were consumed, and the clusters assembled by the rods became larger and more uniform through Ostwald ripening [37]. Consequently, 3D rod clusters were obtained.

3.2 Electrochemical performance in SIBs

The electrochemical performance of $FeSe_2$ electrodes was tested in 1.0 M $NaCF_3SO_3$ in DIGLYME. The charge–discharge profiles (1st, 30th, 100th, 200th, 300th, and 400th cycles) of the as-prepared $FeSe_2$ clusters at 1 $A{\cdot}g^{-1}$ are shown in Fig. 3(a). During the first sodiation process, an obvious voltage plateau was observed around 1.35 V. This is attributed to the slow reaction kinetics and the intercalation and conversion reactions that simultaneously occurred during the first discharge process, which have been previously reported [45–48]. Figure 3(b) shows the cycling performance of the $FeSe_2$ clusters and particles at a current density of 500 $mA{\cdot}g^{-1}$. Notably, the initial Coulombic efficiency of the $FeSe_2$ clusters reached 97.2%. The high Coulombic efficiency is attributed to the high cutoff voltage, which allows the avoidance of the irreversible capacity in the voltage range of 0.5–0 V, according to published reports [49]. Moreover, the as-prepared $FeSe_2$ clusters exhibited high capacity retention of nearly 100% after a few cycles of activation. Clearly, the $FeSe_2$ clusters exhibited a higher capacity and better cycling stability than the $FeSe_2$ particles. After 100 cycles, the $FeSe_2$ clusters retained a capacity of 508 $mAh{\cdot}g^{-1}$, which is significantly higher than that for the $FeSe_2$ particles (389 $mAh{\cdot}g^{-1}$). The long-life cycling performance of the as-prepared $FeSe_2$ was investigated at 1 and 3 $A{\cdot}g^{-1}$ (Fig. 3(c) and Fig. S7 in the ESM, respectively). The as-prepared $FeSe_2$ exhibited a high initial Coulombic efficiency of 97.4% and a discharge capacity of 515 $mAh{\cdot}g^{-1}$ after 400 cycles at 1 $A{\cdot}g^{-1}$. At a high current density of 3 $A{\cdot}g^{-1}$, the $FeSe_2$-cluster electrode retained a capacity of >425 $mAh{\cdot}g^{-1}$ with a Coulombic efficiency of ~100% for 200 cycles.

The rate performances of the as-prepared $FeSe_2$ clusters and particles were investigated by changing the current density from 1 to 35 $A \cdot g^{-1}$, as shown in Fig. 3(d). Because the capacity remained stable after 50 cycles, the rate performance was tested after 50 cycles at 1 $A \cdot g^{-1}$. The average discharge capacities of the as-prepared $FeSe_2$ clusters were 510, 436, 410, 368, 280, 235, 183, and 128 $mAh \cdot g^{-1}$ at current densities of 1, 3, 5, 10, 20, 25, 30, and 35 $A \cdot g^{-1}$, respectively. When the current density returned to 1 $A \cdot g^{-1}$, the capacity increased to the original value. In contrast, the capacities of the $FeSe_2$ particles were only 420, 350, 318, 243, 100, 37, 42, and 40 $mAh \cdot g^{-1}$ at the current densities of 1, 3, 5, 10, 20, 25, 30, and 35 $A \cdot g^{-1}$, respectively. These results indicate that the $FeSe_2$ clusters composed of the nanorods had better cycling capacity and rate performance than the $FeSe_2$ particles.

EIS was performed to identify the reason for the enhanced electrochemical performance of the as-prepared $FeSe_2$ clusters. The results are shown in Fig. 3(e), revealing that the resistances of the electrolyte and cell components (R_s), the resistance of the solid electrolyte interface (R_{SEI}), and the charge-transfer resistance (R_{ct}) of the $FeSe_2$ clusters were smaller than those of the $FeSe_2$ particles, indicating the faster kinetics of the $FeSe_2$ clusters (Table S1 in the ESM). Fast electron/ion transfer kinetics is beneficial for improving the electrochemical performance of electrodes [50–52].

To investigate the effect of the electrolyte parameters on the cycling capability of the electrodes, different electrolytes (1 M $NaClO_4$ in EC/DMC, EC/DMC-5%FEC) were used to study the cycling performance of the as-prepared $FeSe_2$ clusters (Fig. S8 in the ESM). The as-prepared $FeSe_2$ clusters with carbonate-based electrolytes ($NaClO_4$ in EC/DMC, EC/DMC-5%FEC) suffered from rapid capacity decay (8 and 128 $mAh \cdot g^{-1}$ after 100 cycles at 500 $mA \cdot g^{-1}$, respectively). The appropriate ether-based electrolyte effectively suppressed the side reactions between the electrolyte and the anionic groups, improving the cycling performance of the electrodes [38, 53]. Figure S9 in the ESM shows the EIS results for the as-prepared $FeSe_2$ clusters in carbonate-based electrolytes. The resistances of the $FeSe_2$ clusters in the carbonate-based electrolytes were larger than those for the ether-based electrolyte, indicating the slower kinetics.

To explain the high electrochemical performance of the $FeSe_2$ clusters, CV curves for the $FeSe_2$ clusters and particles were obtained at different scan rates ranging from 0.2 to 1 $mV \cdot s^{-1}$ (Fig. 4(a) and Fig. S10

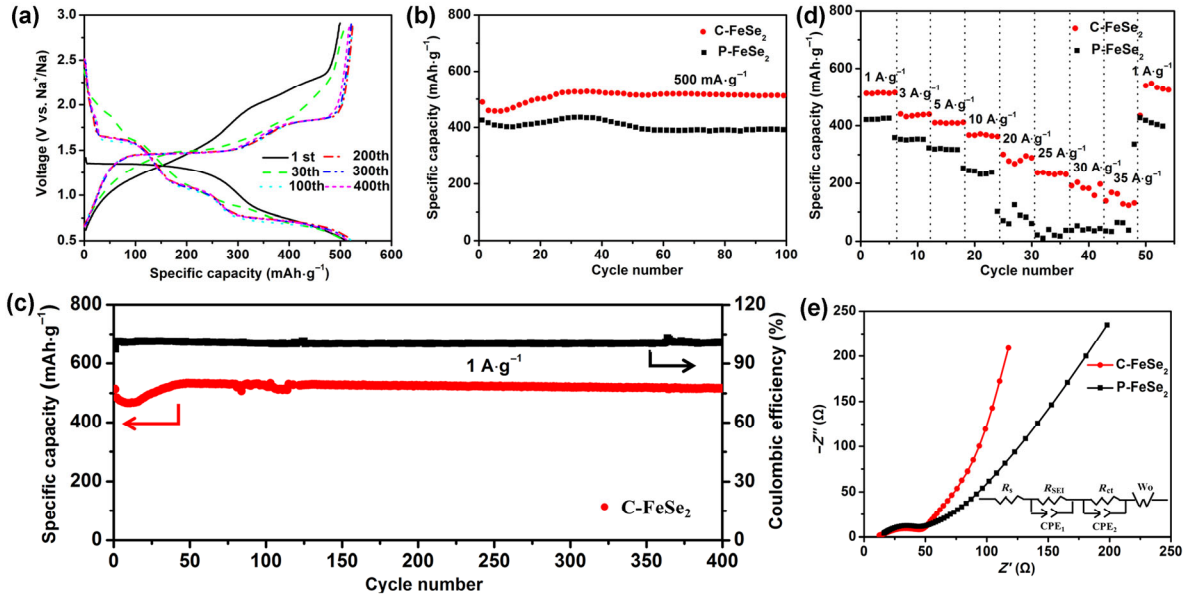

Figure 3 Electrochemical performance of the as-prepared $FeSe_2$ electrodes for SIBs. (a) Charge–discharge profiles of the $FeSe_2$ clusters at a current density of 1 $A \cdot g^{-1}$. (b) Cycling performance of the $FeSe_2$ clusters and particles at 500 $mA \cdot g^{-1}$. (c) Long-life cycling performance of the $FeSe_2$ clusters at 1 $A \cdot g^{-1}$. (d) Rate performance of the $FeSe_2$ clusters and particles after 50 cycles at current densities ranging from 1 to 35 $A \cdot g^{-1}$. (e) Nyquist plots for the $FeSe_2$ clusters and particles.

in the ESM). The CV curves for the $FeSe_2$ clusters overlapped to a greater degree than those of the $FeSe_2$ particles at different scan rates, indicating the better cycle reversibility of the $FeSe_2$ clusters. The sodium-diffusion coefficient was calculated using the Randles–Sevick equation [54, 55]

$$I_p = 0.4463nFAC(nFvD/RT)^{1/2} = [(269000)n^{3/2}AD^{1/2}C]v^{1/2} \quad (1)$$

where I_p is the peak current, n is the number of electrons transferred in the redox process, F is Faraday's constant, A is the surface area of the electrode, D is the diffusion coefficient, C is the concentration of sodium ions, and v is the scan rate. Using Eq. (1), the plot of the peak current I_p vs. the square root of the scan rate ($v^{1/2}$) was obtained for the peak oxidation current at a voltage of 1.52 V (Fig. 4(b)). The calculated diffusion coefficient D for the $FeSe_2$ clusters (1.32×10^{-8} $cm^2 \cdot s^{-1}$) was significantly greater than that for the $FeSe_2$ particles (6.1×10^{-10} $cm^2 \cdot s^{-1}$). Moreover, this value is greater than that commonly reported for anodes used in SIBs [56, 57], indicating the potential of the $FeSe_2$ clusters for high-rate applications.

To provide insights and quantify the total capacitive contribution in the material, the capacitive and diffusion contributions were separated at a fixed voltage according to the following equation

$$i\,(V) = k_1v + k_2v^{1/2} \quad (2)$$

where k_1v and $k_2v^{1/2}$ represent the capacitive and diffusion contributions, respectively. Figure 4(c) shows the separation of the capacitive and diffusion currents of the $FeSe_2$ clusters at a scan rate of 0.6 $mV \cdot s^{-1}$. The quantification results indicate that 72.6% of the total charge storage was capacitive. The ratios of the capacitive contribution to the diffusion contribution at different scan rates are presented in Fig. 4(d). The capacitive contribution gradually increased as the scan rate increased. At a scan rate of 0.8 $mV \cdot s^{-1}$, the capacitive-contribution ratio was 89.4%. A large capacitive contribution was beneficial for fast charge storage and yielded the high rate capability of the $FeSe_2$ clusters. This capacitive behavior is similar to that previously reported [11, 43].

To investigate the reaction kinetics of Na/$FeSe_2$ cells, EIS was performed on an electrode comprising

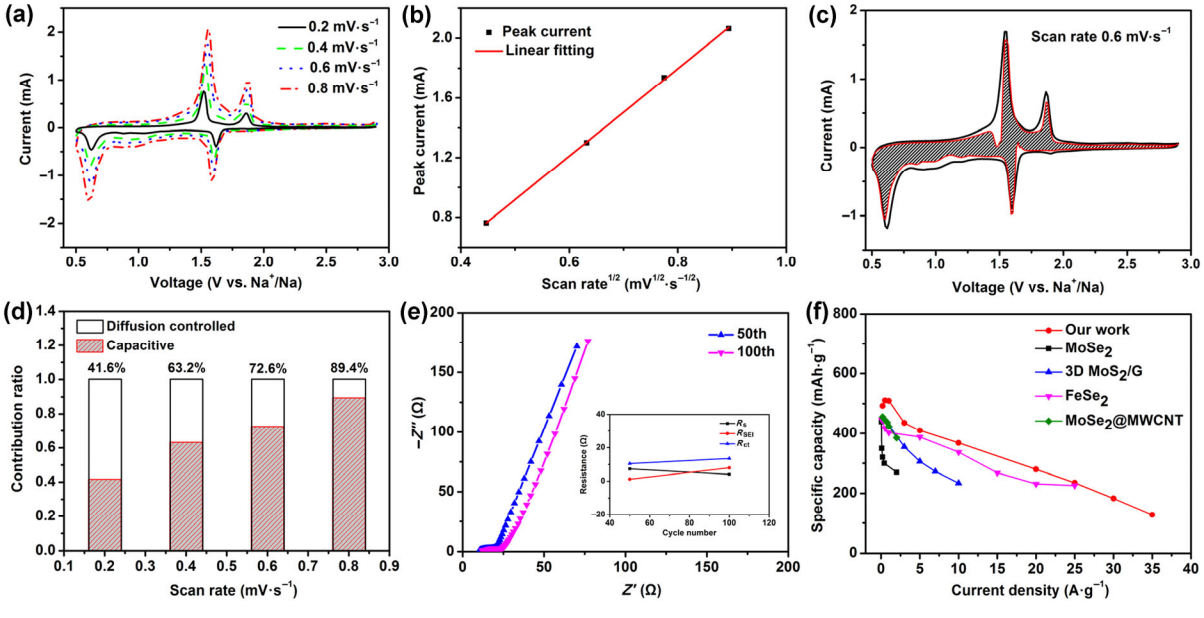

Figure 4 (a) CV curves of the as-prepared $FeSe_2$ clusters at different scan rates after 50 cycles. (b) Randles–Sevick plot for the as-prepared $FeSe_2$ clusters obtained from the CV data. (c) Separation of the capacitive and diffusion currents in the $FeSe_2$ clusters at a scan rate of 0.6 $mV \cdot s^{-1}$. (d) Contribution ratio of the capacitive and diffusion-controlled charge storage in the $FeSe_2$ clusters at 0.2, 0.4, 0.6, and 0.8 $mV \cdot s^{-1}$. (e) Nyquist plots for the as-prepared $FeSe_2$ electrode in the fully charged state after cycling from 1st to 100th. (d) Impedances R_s, R_{SEI}, and R_{ct} of the $FeSe_2$ electrode during cycling. (f) Comparison between other SIB anode materials and the material proposed herein.

as-prepared $FeSe_2$ clusters in the fully charged state after cycling (Fig. 4(e)). The as-prepared $FeSe_2$-cluster electrode exhibited stable values of R_s, R_{SEI}, and R_{ct} after 50 cycles (inset of Fig. 4(e)), indicating the highly stable electrochemical process. Figure 4(f) compares the rate performance of the as-prepared $FeSe_2$ clusters with those of other anode materials for SIBs [30–32, 38]. Clearly, the $FeSe_2$ clusters had a higher capacity and better rate performance than the other anode materials.

In situ XRD was performed to further investigate the intrinsic reaction mechanisms of the $FeSe_2$-cluster electrodes. An *in situ* cell was discharged to 0.5 V and then charged to 2.9 V under a constant current of 100 $mA{\cdot}g^{-1}$ at room temperature (Fig. S11 in the ESM). During the first discharge process, there were three diffraction peaks (30.89°, 34.83°, and 36.23°), which correspond to the (020), (111), and (120) planes of $FeSe_2$, respectively. During the reaction, these peaks became weaker and then disappeared. No obvious diffraction peaks appeared in the subsequent charge and discharge process. These results indicate that the amorphization of the $FeSe_2$ electrode occurred after the electrochemical sodium-ion insertion.

According to the aforementioned results, the excellent electrochemical performance of the as-prepared $FeSe_2$ clusters was due to the unique 3D structure, the highly capacitive behavior, and the appropriate ether-based electrolyte. The unique 3D structure enhanced the electron/ion-transfer kinetics. The highly capacitive behavior was beneficial for fast charge storage. The appropriate ether-based electrolyte suppressed the side reactions between the electrolyte and the anionic group of the intermediate, enhancing the cycling performance of the as-prepared $FeSe_2$-clusters electrode.

4 Conclusions

We successfully synthesized 3D $FeSe_2$ clusters composed of nanorods using a facile hydrothermal method. As an anode material for SIBs, the as-prepared $FeSe_2$ clusters exhibited excellent cycling performance and a rate capability as high as 35 $A{\cdot}g^{-1}$. They delivered a high initial Coulombic efficiency of 97.4% and a high discharge capacity of 515 $mAh{\cdot}g^{-1}$ after 400 cycles at 1 $A{\cdot}g^{-1}$. Furthermore, we demonstrated that the unique 3D structure, highly capacitive behavior, and appropriate ether-based electrolyte contributed to the high electrochemical performance. The excellent overall performance of the $FeSe_2$ clusters makes them a promising anode material for SIBs.

Acknowledgements

This work was supported by the National Key Research and Development Program of China (No. 2016YFA0202603), the National Natural Science Foundation of China (Nos. 51425204 and 51602239), the Hubei Provincial Natural Science Foundation of China (No. 2016CFB267), the Fundamental Research Funds for the Central Universities (Nos. 2016IVA090 and 2017III005), the Natural Science Foundation of Henan Province (Nos. 152300410114 and 14B140009), the China Postdoctoral Science Foundation (No. 2016M592401). L. Q. M. gratefully acknowledged financial support from China Scholarship Council (No. 201606955096).

Electronic Supplementary Material: Supplementary material (XRD pattern of as-prepared $FeSe_2$ particles; the low-magnification SEM image of obtained $FeSe_2$ clusters; elemental mapping images and EDS pattern of the as-prepared $FeSe_2$ clusters; the low- and high-magnification SEM images of as-prepared $FeSe_2$ particles, respectively; SEM images of as-prepared $FeSe_2$ clusters obtained at different times: 1, 3, 6 and 8 h; schematic illustration for the fabrication process of $FeSe_2$ clusters; the cycling performance of $FeSe_2$ clusters at a current density of 3 $A{\cdot}g^{-1}$; the cycling performance of $FeSe_2$ clusters in different electrolytes at a current density of 500 $mA{\cdot}g^{-1}$; Nyquist plots of $FeSe_2$ clusters in different electrolytes; CV curves of as-prepared $FeSe_2$ particles at different scan rates and Randles–Sevick plot of $FeSe_2$ particles obtained from CV data; *in situ* XRD patterns collected during galvanostatic charge/discharge of $FeSe_2$ clusters within 0.5–2.9 V; resistances value by fitting EIS results) is available in the online version of this article at https://doi.org/10.1007/s12274-017-1537-z.

References

[1] Mahmood, N.; Zhang, C. Z.; Liu, F.; Zhu, J. H.; Hou, Y. L. Hybrid of Co_3Sn_2@Co nanoparticles and nitrogen-doped

graphene as a lithium ion battery anode. *ACS Nano* **2013**, *7*, 10307–10318.

[2] Xu, Y. H.; Zhu, Y. J.; Liu, Y. H.; Wang, C. S. Electrochemical performance of porous carbon/tin composite anodes for sodium-ion and lithium-ion batteries. *Adv. Energy Mater.* **2013**, *3*, 128–133.

[3] Wu, C.; Maier, J.; Yu, Y. Sn-based nanoparticles encapsulated in a porous 3D graphene network: Advanced anodes for high-rate and long life Li-ion batteries. *Adv. Funct. Mater.* **2015**, *25*, 3488–3496.

[4] Raju, V.; Rains, J.; Gates, C.; Luo, W.; Wang, X. F.; Stickle, W. F.; Stucky, G. D.; Ji, X. L. Superior cathode of sodium-ion batteries: Orthorhombic V_2O_5 nanoparticles generated in nanoporous carbon by ambient hydrolysis deposition. *Nano Lett.* **2014**, *14*, 4119–4124.

[5] Chen, Z.; Augustyn, V.; Jia, X. L.; Xiao, Q. F.; Dunn, B.; Lu, Y. F. High-performance sodium-ion pseudocapacitors based on hierarchically porous nanowire composites. *ACS Nano* **2012**, *6*, 4319–4327.

[6] Sun, J.; Lee, H. W.; Pasta, M.; Yuan, H. T.; Zheng, G. Y.; Sun, Y. M.; Li, Y. Z.; Cui, Y. A phosphorene-graphene hybrid material as a high-capacity anode for sodium-ion batteries. *Nat. Nanotechnol.* **2015**, *10*, 980–985.

[7] Hong, S. Y.; Kim, Y.; Park, Y.; Choi, A.; Choi, N. S.; Lee, K. T. Charge carriers in rechargeable batteries: Na ions vs. Li ions. *Energy Environ. Sci.* **2013**, *6*, 2067–2081.

[8] Darwiche, A.; Marino, C.; Sougrati, M. T.; Fraisse, B.; Stievano, L.; Monconduit, L. Better cycling performances of bulk Sb in Na-ion batteries compared to Li-ion systems: An unexpected electrochemical mechanism. *J. Am. Chem. Soc.* **2012**, *134*, 20805–20811.

[9] Kim, Y.; Kim, Y.; Choi, A.; Woo, S.; Mok, D.; Choi, N. S.; Jung, Y. S.; Ryu, J. H.; Oh, S. M.; Lee, K. T. Tin phosphide as a promising anode material for Na-ion batteries. *Adv. Mater.* **2014**, *26*, 4139–4144.

[10] Liang, L. Y.; Xu, Y.; Wang, C. L.; Wen, L. Y.; Fang, Y. G.; Mi, Y.; Zhu, M.; Zhao, H. P.; Lei, Y. Large-scale highly ordered Sb nanorod array anodes with high capacity and rate capability for sodium-ion batteries. *Energy Environ. Sci.* **2015**, *8*, 2954–2962.

[11] Hu, Z.; Zhu, Z. Q.; Cheng, F. Y.; Zhang, K.; Wang, J. B.; Chen, C. C.; Chen, J. Pyrite FeS_2 for high-rate and long-life rechargeable sodium batteries. *Energy Environ. Sci.* **2015**, *8*, 1309–1316.

[12] Wang, L. J.; Zhang, K.; Hu, Z.; Duan, W. C.; Cheng, F. Y.; Chen, J. Porous CuO nanowires as the anode of rechargeable Na-ion batteries. *Nano Res.* **2014**, *7*, 199–208.

[13] Saravanan, K.; Mason, C. W.; Rudola, A.; Wong, K. H.; Balaya, P. The first report on excellent cycling stability and superior rate capability of $Na_3V_2(PO_4)_3$ for sodium ion batteries. *Adv. Energy Mater.* **2013**, *3*, 444–450.

[14] Dong, Y. F.; Li, S.; Zhao, K. N.; Han, C. H.; Chen, W.; Wang, B. L.; Wang, L.; Xu, B. A.; Wei, Q. L.; Zhang, L. et al. Hierarchical zigzag $Na_{1.25}V_3O_8$ nanowires with topotactically encoded superior performance for sodium-ion battery cathodes. *Energy Environ. Sci.* **2015**, *8*, 1267–1275.

[15] Barpanda, P.; Oyama, G.; Nishimura, S.; Chung, S. C.; Yamada, A. A 3.8-V earth-abundant sodium battery electrode. *Nat. Commun.* **2014**, *5*, 4358.

[16] You, Y.; Wu, X. L.; Yin, Y. X.; Guo, Y. G. High-quality Prussian blue crystals as superior cathode materials for room-temperature sodium-ion batteries. *Energy Environ. Sci.* **2014**, *7*, 1643–1647.

[17] Cao, Y. L.; Xiao, L. F.; Sushko, M. L.; Wang, W.; Schwenzer, B.; Xiao, J.; Nie, Z. M.; Saraf, L. V.; Yang, Z. G.; Liu, J. Sodium ion insertion in hollow carbon nanowires for battery applications. *Nano Lett.* **2012**, *12*, 3783–3787.

[18] Zhao, J.; Zhao, L. W.; Chihara, K.; Okada, S.; Yamaki, J. I.; Matsumoto, S.; Kuze, S.; Nakane, K. Electrochemical and thermal properties of hard carbon-type anodes for Na-ion batteries. *J. Power Sources* **2013**, *244*, 752–757.

[19] Dahbi, M.; Yabuuchi, N.; Kubota, K.; Tokiwa, K.; Komaba, S. Negative electrodes for Na-ion batteries. *Phys. Chem. Chem. Phys.* **2014**, *16*, 15007–15028.

[20] Ponrouch, A.; Marchante, E.; Courty, M.; Tarascon, J. M.; Palacin, M. R. In search of an optimized electrolyte for Na-ion batteries. *Energy Environ. Sci.* **2012**, *5*, 8572–8583.

[21] Komaba, S.; Murata, W.; Ishikawa, T.; Yabuuchi, N.; Ozeki, T.; Nakayama, T.; Ogata, A.; Gotoh, K.; Fujiwara, K. Electrochemical Na insertion and solid electrolyte interphase for hard-carbon electrodes and application to Na-ion batteries. *Adv. Funct. Mater.* **2011**, *21*, 3859–3867.

[22] Liu, Y. C.; Zhang, N.; Jiao, L. F.; Tao, Z. L.; Chen, J. Ultrasmall Sn nanoparticles embedded in carbon as high-performance anode for sodium-ion batteries. *Adv. Funct. Mater.* **2015**, *25*, 214–220.

[23] Abel, P. R.; Lin, Y. M.; de Souza, T.; Chou, C. Y.; Gupta, A.; Goodenough, J. B.; Hwang, G. S.; Heller, A.; Mullins, C. B. Nanocolumnar germanium thin films as a high-rate sodium-ion battery anode material. *J. Phys. Chem. C* **2013**, *117*, 18885–18890.

[24] Qian, J. F.; Wu, X. Y.; Cao, Y. L.; Ai, X. P.; Yang, H. X. High capacity and rate capability of amorphous phosphorus for sodium ion batteries. *Angew. Chem., Int. Ed.* **2013**, *125*, 4731–4734.

[25] He, M.; Kravchyk, K.; Walter, M.; Kovalenko, M. V. Monodisperse antimony nanocrystals for high-rate Li-ion and Na-ion battery anodes: Nano versus bulk. *Nano Lett.*

2014, *14*, 1255–1262.

[26] Zhang, N.; Han, X. P.; Liu, Y. C.; Hu, X. F.; Zhao, Q.; Chen, J. 3D porous γ-Fe_2O_3@C nanocomposite as high-performance anode material of Na-ion batteries. *Adv. Energy Mater.* **2015**, *5*, 1401123.

[27] Lu, Y. C.; Ma, C. Z.; Alvarado, J.; Dimov, N.; Meng, Y. S.; Okada, S. Improved electrochemical performance of tin-sulfide anodes for sodium-ion batteries. *J. Mater. Chem. A* **2015**, *3*, 16971–16977.

[28] Sun, W. P.; Rui, X. H.; Yang, D.; Sun, Z. Q.; Li, B.; Zhang, W. Y.; Zong, Y.; Madhavi, S.; Dou, S. X.; Yan, Q. Y. Two-dimensional tin disulfide nanosheets for enhanced sodium storage. *ACS Nano* **2015**, *9*, 11371–11381.

[29] Liu, X.; Zhang, K.; Lei, K. X.; Li, F. J.; Tao, Z. L.; Chen, J. Facile synthesis and electrochemical sodium storage of CoS_2 micro/nano-structures. *Nano Res.* **2016**, *9*, 198–206.

[30] Wang, H.; Lan, X. Z.; Jiang, D. L.; Zhang, Y.; Zhong, H. H.; Zhang, Z. P.; Jiang, Y. Sodium storage and transport properties in pyrolysis synthesized $MoSe_2$ nanoplates for high performance sodium-ion batteries. *J. Power Sources* **2015**, *283*, 187–194.

[31] Choi, S. H.; Ko, Y. N.; Lee, J. K.; Kang, Y. C. 3D MoS_2-graphene microspheres consisting of multiple nanospheres with superior sodium ion storage properties. *Adv. Funct. Mater.* **2015**, *25*, 1780–1788.

[32] Zhang, Z. A.; Yang, X.; Fu, Y.; Du, K. Ultrathin molybdenum diselenide nanosheets anchored on multi-walled carbon nanotubes as anode composites for high performance sodium-ion batteries. *J. Power Sources* **2015**, *296*, 2–9.

[33] Xiong, X. Q.; Luo, W.; Hu, X. L.; Chen, C. J.; Long, Q.; Hou, D. F.; Huang, Y. H. Flexible membranes of MoS_2/C nanofibers by electrospinning as binder-free anodes for high-performance sodium-ion batteries. *Sci. Rep.* **2015**, *5*, 9254.

[34] Li, Y. F.; Liang, Y. L.; Hernandez, F. C. R.; Yoo, H. D.; An, Q. Y.; Yao, Y. Enhancing sodium-ion battery performance with interlayer-expanded MoS_2-PEO nanocomposites. *Nano Energy* **2015**, *15*, 453–461.

[35] Wang, W. J.; Pan, X.; Liu, W. Q.; Zhang, B.; Chen, H. W.; Fang, X. Q.; Yao, J. X.; Dai, S. Y. $FeSe_2$ films with controllable morphologies as efficient counter electrodes for dye-sensitized solar cells. *Chem. Commun.* **2014**, *50*, 2618–2620.

[36] Yuan, B. X.; Luan, W. L.; Tu, S. T. One-step synthesis of cubic FeS_2 and flower-like $FeSe_2$ particles by a solvothermal reduction process. *Dalton Trans.* **2012**, *41*, 772–776.

[37] Shi, W. D.; Zhang, X.; Che, G. B.; Fan, W. Q.; Liu, C. B. Controlled hydrothermal synthesis and magnetic properties of three-dimensional $FeSe_2$ rod clusters and microspheres. *Chem. Eng. J.* **2013**, *215–216*, 508–516.

[38] Zhang, K.; Hu, Z.; Liu, X.; Tao, Z. L.; Chen, J. $FeSe_2$ microspheres as a high-performance anode material for Na-ion batteries. *Adv. Mater.* **2015**, *27*, 3305–3309.

[39] Niu, C. J.; Meng, J. S.; Han, C. H.; Zhao, K. N.; Yan, M. Y.; Mai, L. Q. VO_2 nanowires assembled into hollow microspheres for high-rate and long-life lithium batteries. *Nano Lett.* **2014**, *14*, 2873–2878.

[40] Mai, L. Q.; An, Q. Y.; Wei, Q. L.; Fei, J. Y.; Zhang, P. F.; Xu, X.; Zhao, Y. L.; Yan, M. Y.; Wen, W.; Xu, L. Nanoflakes-assembled three-dimensional hollow-porous V_2O_5 as lithium storage cathodes with high-rate capacity. *Small* **2014**, *10*, 3032–3037.

[41] Han, C. H.; Pi, Y. Q.; An, Q. Y.; Mai, L. Q.; Xie, J. L.; Xu, X.; Xu, L.; Zhao, Y. L.; Niu, C. J.; Khan, A. M. et al. Substrate-assisted self-organization of radial β-$AgVO_3$ nanowire clusters for high rate rechargeable lithium batteries. *Nano Lett.* **2012**, *12*, 4668–4673.

[42] Augustyn, V.; Come, J.; Lowe, M. A.; Kim, J. W.; Taberna, P. L.; Tolbert, S. H.; Abruña, H. D.; Simon, P.; Dunn, B. High-rate electrochemical energy storage through Li^+ intercalation pseudocapacitance. *Nat. Mater.* **2013**, *12*, 518–522.

[43] Chen, C. J.; Wen, Y. W.; Hu, X. L.; Ji, X. L.; Yan, M. Y.; Mai, L. Q.; Hu, P.; Shan, B.; Huang, Y. H. Na^+ intercalation pseudocapacitance in graphene-coupled titanium oxide enabling ultra-fast sodium storage and long-term cycling. *Nat. Commun.* **2015**, *6*, 6929.

[44] Yu, P. F.; Li, C. L.; Guo, X. X. Sodium storage and pseudocapacitive charge in textured $Li_4Ti_5O_{12}$ thin films. *J. Phys. Chem. C* **2014**, *118*, 10616–10624.

[45] Zhu, Y. J.; Fan, X. L.; Suo, L. M.; Luo, C.; Gao, T.; Wang, C. S. Electrospun FeS_2@carbon fiber electrode as a high energy density cathode for rechargeable lithium batteries. *ACS Nano* **2016**, *10*, 1529–1538.

[46] Son, S. B.; Yersak, T. A.; Piper, D. M.; Kim, S. C.; Kang, C. S.; Cho, J. S.; Suh, S. S.; Kim, Y. U.; Oh, K. H.; Lee, S. H. A stabilized PAN-FeS_2 cathode with an EC/DEC liquid electrolyte. *Adv. Energy Mater.* **2014**, *4*, 1300961.

[47] Kitajou, A.; Yamaguchi, J.; Hara, S.; Okada, S. Discharge/charge reaction mechanism of a pyrite-type FeS_2 cathode for sodium secondary batteries. *J. Power Sources* **2014**, *247*, 391–395.

[48] Liu, J.; Wen, Y. R.; Wang, Y.; van Aken, P. A.; Maier, J.; Yu, Y. Carbon-encapsulated pyrite as stable and earth-abundant high energy cathode material for rechargeable lithium batteries. *Adv. Mater.* **2014**, *26*, 6025–6030.

[49] Kim, H.; Hong, J.; Park, Y. U.; Kim, J.; Hwang, I.; Kang, K. Sodium storage behavior in natural graphite using ether-based electrolyte systems. *Adv. Funct. Mater.* **2015**, *25*, 534–541.

[50] Wei, X. J.; An, Q. Y.; Wei, Q. L.; Yan, M. Y.; Wang, X. P.; Li, Q. D.; Zhang, P. F.; Wang, B. L.; Mai, L. Q. A bowknot-like RuO_2 quantum dots@V_2O_5 cathode with largely improved electrochemical performance. *Phys. Chem. Chem. Phys.* **2014**, *16*, 18680–18685.

[51] Wei, X. J.; Tang, C. J.; Wang, X. P.; Zhou, L.; Wei, Q. L.; Yan, M. Y.; Sheng, J. Z.; Hu, P.; Wang, B. L.; Mai, L. Q. Copper silicate hydrate hollow spheres constructed by nanotubes encapsulated in reduced graphene oxide as long-life lithium-ion battery anode. *ACS Appl. Mater. Interfaces* **2015**, *7*, 26572–26578.

[52] Wei, Q. L.; An, Q. Y.; Chen, D. D.; Mai, L. Q.; Chen, S. Y.; Zhao, Y. L.; Hercule, K. M.; Xu, L.; Khan, A. M.; Zhang, Q. J. One-pot synthesized bicontinuous hierarchical $Li_3V_2(PO_4)_3$/C mesoporous nanowires for high-rate and ultralong-life lithium-ion batteries. *Nano Lett.* **2014**, *14*, 1042–1048.

[53] Gao, J.; Lowe, M. A.; Kiya, Y.; Abruña, H. D. Effects of liquid electrolytes on the charge–discharge performance of rechargeable lithium/sulfur batteries: Electrochemical and *in-situ* X-ray absorption spectroscopic studies. *J. Phys. Chem. C* **2011**, *115*, 25132–25137.

[54] Jung, H. G.; Hassoun, J.; Park, J. B.; Sun, Y. K.; Scrosati, B. An improved high-performance lithium–air battery. *Nat. Chem.* **2012**, *4*, 579–585.

[55] Wang, X. P.; Niu, C. J.; Meng, J. S.; Hu, P.; Xu, X. M.; Wei, X. J.; Zhou, L.; Zhao, K. N.; Luo, W.; Yan, M. Y. et al. Novel $K_3V_2(PO_4)_3$/C bundled nanowires as superior sodium-ion battery electrode with ultrahigh cycling stability. *Adv. Energy Mater.* **2015**, *5*, 1500716.

[56] Rudola, A.; Saravanan, K.; Mason, C. W.; Balaya, P. $Na_2Ti_3O_7$: An intercalation based anode for sodium-ion battery applications. *J. Mater. Chem. A* **2013**, *1*, 2653–2662.

[57] Ko, Y. N.; Choi, S. H.; Kang, Y. C. Hollow cobalt selenide microspheres: Synthesis and application as anode materials for Na-ion batteries. *ACS Appl. Mater. Interfaces* **2016**, *8*, 6449–6456.